

LUVOIR Primary Mirror Segment Alignment Control With Joint Laser Metrology and Segment Edge Sensing

John Z Lou, David C Redding, Joel A Nissen and Chris Shelton
Jet Propulsion Laboratory, Caltech, Pasadena, CA 91109

Abstract

An approach is developed for the alignment and stability maintenance of the LUVOIR segmented primary mirror using a segment state estimation and wavefront control method based on a hybrid segment motion sensing architecture of laser truss metrology and segment edge sensors. Our current computer model was generated for LUVOIR Architecture Option A with a 15-meter aperture, 120-segment primary mirror. The methodology and simulation results will be presented and analyzed.

JPL has a long history of technology development in laser metrology and edge sensors, including work in SIM [7], Keck and TMT [8], CCAT [3] and LUVOIR [1]. We will discuss our current efforts of LUVOIR laser metrology and edge-sensor models development, showing sensitivities of sensor measurements to various mirror eigenmodes, removing global modes and strengthening weak modes by performing joint (hybrid) laser-metrology and edge sensing. We will define and derive an important performance metric called *wavefront error multiplier* (*WEM*), and show that *WEM* provides a simple link between sensor errors and the closed-loop (controlled) system wavefront error. We will show *WEM* values for several hybrid sensor configuration options studied.

We will discuss an algorithm for mirror shape control and maintenance through segment state and wavefront estimations using joint edge-metrology sensing. We will compare simulated performance of mirror state estimation, wavefront estimation and wavefront control based on joint edge-metrology sensing among several sensor configurations, and show the impact of sensor error distributions on the segmented mirror alignment performance. Mirror shape control performance will be also be evaluated in terms of imaging contrast between inner working angles (IWA) and outer working angles (OWA) of a LUVOIR coronagraph.

The research was carried out at the Jet Propulsion Laboratory, California Institute of Technology, under a contract with the National Aeronautics and Space Administration. LUVOIR is a mission concept under study for the next astronomy Decadal Survey—the information presented in this paper is pre-decisional and is provided for planning and discussion purposes only.

Copyright 2018 California Institute of Technology. U.S. Government sponsorship is acknowledged.

1. Introduction

LUVOIR’s exoplanet observations would be accomplished by *high optical resolution* offered by a large segmented aperture, and *high contrast direct imaging* using a coronagraph to block the light from a star in order to detect and characterize the much fainter light reflected from planets orbiting the star. The optical layout of a canonical coronagraph [1] is sketched in Fig 1. The wavefront requirement for exoplanet observations falls in the range of pico-meters in order to realize the planet-star contrast of the order of 10^{-10} , which is needed to have an IWA of a few λ/D , where λ and D are coronagraph central wavelength and the telescope main aperture, respectively. This performance requirement calls for ultra-stability of the primary mirror and highly robust and accurate wavefront sensing and control mechanisms.

Since no single approach would be sufficient to achieve the wavefront and contrast performance required for exoplanet observations, the LUVOIR technology development is currently exploring a set of existing and new promising technologies and seeks to use a combination of them for implementing a

successful LUVOIR mission. Exit pupil wavefront sensing, drawing on the heritage of James Webb Space Telescope (JWST) [6] and work from other NASA/DoD missions, provides a very accurate means of measuring the total effect of optical system aberrations on the imaging quality. Iterative wavefront sensing algorithms such as MGS [6] or image-based parametric algorithms can work effectively with segmented aperture systems as a fine-phasing step to generate accurate system wavefront estimates.

Interferometric wavefront sensors such as low-order (Zernike) wavefront sensors (LOWFS) have been known in theory and demonstrated in testbeds such as those for proposed WFIRST observatory [4] to be able to provide an accurate means of continuously sensing and control low-order wavefront modes such as telescope pointing errors and wavefront errors (WFE) due to changes of thermal environment for a system with a monolithic aperture. ZWFS can effectively sense low-order spatial modes in the wavefront since it uses a reference beam reflected from the coronagraph occulting core. More recent work on Out-of-Band WF sensor (OBWFS) [5], still based on the ZWFS interferometric architecture, performs WF sensing using UV light of the entire star light beam, so that all of the WF spatial frequencies can be measured and controlled.

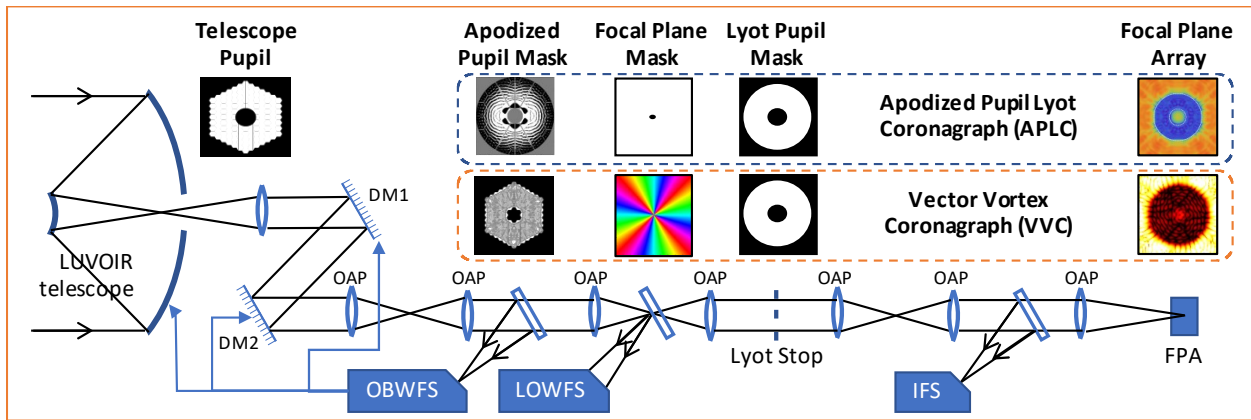


Figure 1: A canonical LUVOIR coronagraph system design

Another powerful tool to meet the LUVOIR ultra-stability requirement would be high bandwidth metrology of the telescope optical alignments. Coupled with precision rigid-body actuator (RBA) control, optical metrology enables rapidly stabilizing and maintaining the position and orientation of each optic or telescope assembly relative to each other or to some reference point. A significant advantage of using metrology for LUVOIR optical alignment is that it does not require a guide star to sense and control the largest sources of instability, such as dephasing of the PM segments and position and orientation errors of the secondary mirror. Metrology is therefore complementary to wavefront sensors such as MGS, LOWFS and OBWFS, providing much higher bandwidth maintenance of telescope configuration during maneuvers, and ensuring telescope performance during astrophysical sciences observations when the coronagraph is not operating.

This paper focuses on two metrology methods especially well-suited for LUVOIR. The first is Laser Truss Metrology (LMET), which uses a set of laser distance gauges, such as beam launchers (BL) and corner cubes (CC) to form a round-trip laser path, to measure the changes of rigid body state of the primary mirror segments relative to the secondary mirror, and the change of secondary mirror state relative to the instrument optics behind the primary mirror as depicted in Fig 2. LMET can measure the alignment of all of the major optical elements relative to a common reference, such as the attitude control system platform. The sensitivity *strength* of a LMET system depends on the beam configuration of BL and CC. A pose error multiplier vector can be computed for a given LMET configuration, which shows the estimated segment pose errors for a unit of metrology sensor error. When system wavefront is the driving performance metric, a convenient metric for the LMET sensitivity strength is a scalar value called *Wavefront Error Multiplier (WEM)*, which is obtained by projecting the pose error multiplier into the

wavefront space. A design goal of a LUVOIR LMET system is to minimize the WEM subject to other engineering constraints.

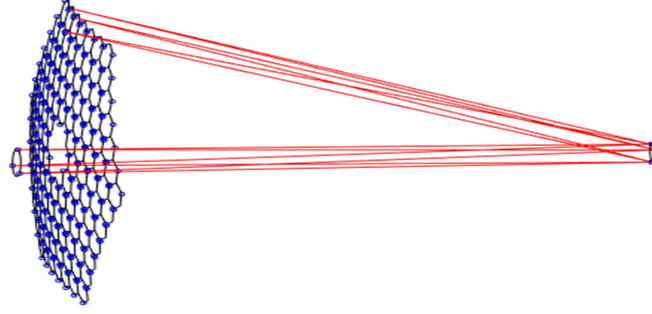


Figure 2: Laser metrology beams between primary segments to secondary, and secondary to instrument bench behind primary

The second metrology method is Segment Edge Sensors (SES), using high precision three-dimensional measurements of the change of relative positions of a pair of adjacent segment edges, made typically at two locations along each edge. Capacitive sensors have been used for segmented ground telescopes. The Keck Observatory on Mauna Kea implemented interleaved sensing elements with 1 nm measurement noise. Capacitive gap measurement devices have demonstrated 15 pm precision for applications on the Laser Interferometer Space Antenna (LISA) mission with very small gap between segments. Edge sensors planned for the upcoming Thirty Meter Telescope use face-on sensing plates, plus gap measurements, non-interleaved approach better suited for deployed-aperture space telescopes (Shelton 2008) [8]. Other edge sensor designs, using inductive or optical measurements have been studied (Burt 2012) [9].

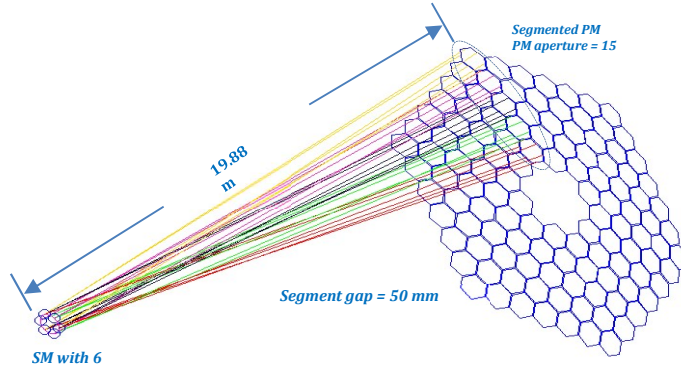


Figure 3: LUVOIR primary laser truss metrology model developed in our study

A SES system generates different sensitivity *strength* corresponding to different mirror *eigen-mode*. And, similarly, a WEM can be computed for a given SES system. A more detailed SES description and analysis are presented in Section 3. Since SES measurements are between a pair of segment edges, it is obvious that SES does not generate any response to rigid body motions of the entire mirror; in addition, SES generates very weak responses to low-order mirror eigenmodes (such as focus mode). A combination of LMET and SES provides the potential of a metrology system with better performance than using either one of them, simpler structure and reasonable cost. Hybrid metrology system options are discussed in Section 4.

A closed loop control system feeds back the LMET and SES measurements to segment Rigid Body Actuators (RBAs) to keep the segments aligned to each other. One approach is to perform wavefront control through a segment state estimator based on metrology measurements. Since wavefront is directly

related to system imaging performance, it makes sense to drive the controller to minimize the estimated wavefront error. Segment state estimation, state and wavefront estimates and wavefront control are discussed in Section 5.

2. LUVOIR Primary Truss Metrology Model and Sensitivity

LMET draws its heritage from NASA's Space Interferometry Mission (SIM) project, which demonstrated pico-meter precision on large ground-based testbeds with large and heavy beam launchers and corner cubes [7]. Subsequent development at JPL achieved much smaller and more compact LMET devices, for attachment to lightweight mirror segments, targeting performance at the sub-nanometer level. LISA Pathfinder has further refined laser metrology technology with laser gauges and electronics that achieve picometer accuracy. LUVOIR metrology development aims to combine SIM and LISA LMET approaches to provide picometer-precision measurements, with a compact and unobtrusive LMET package, that LUVOIR would need to preserve coronagraph high contrast performance during extended science observations.

To model and analyze LMET performance on LUVOIR architecture A, an optical system model with a 15-meter primary mirror (PM) of 120 segments is generated using a JPL-developed optical modeling tool called MACOS (Modeling and Analysis of Controlled Optical Systems). The optical system model is then used to generate linear model sensitivities for system wavefront and laser metrology measurements. A rigid-body PM segment pose state consists of six degrees of freedom (6DOF), with three rotations and three translations defined in each segment's local coordinate frame. Wavefront sensitivities are generated with respect to the change of segment rigid-body state, which is used to generate estimated linear wavefront given a PM segment state estimate. A linear wavefront due to segment state change can be expressed using wavefront sensitivities

$$W = W_0 + dwdx * dx \quad (1)$$

where W_0 is the design wavefront residual, $dwdx$ is the wavefront sensitivity matrix, and dx is the change of segment state vector. With LMET, the PM segment state is related to the laser metrology measurements by

$$dx = pinv(dldx) * dl \quad (2)$$

where dl is the changes of round-trip metrology leg length between BL and CC due to changes of segment poses dx , $dldx$ is the sensitivity matrix linking segment poses to metrology leg lengths, and $pinv()$ is the pseudo-inverse operator. The $dldx$ matrix is generated with MACOS by perturbing each DOF of a segment in its local coordinate frame and calculating the change of metrology leg length. Given a set of laser metrology measurements dl , the estimated wavefront, using a simple least-square approach, can then be obtained by combining (1) and (2)

$$dW = dwdx * pinv(dldx) * dl \quad (3)$$

where $dW = W - W_0$ is the wavefront change due to segment pose change. The accuracy of the wavefront estimate dW depends on the accuracy of the metrology measurements dl as shown in (3). Suppose metrology has measurement errors η , the noise metrology measurement vector is then

$$dl^\wedge = dl + \eta$$

The error of estimated wavefront due to metrology error is given by

$$dW^\wedge = dwdx * pinv(dldx) * \eta \quad (4)$$

Equation (4) indicates that dW^\wedge is directly affected by the *conditioning* of matrix $dldx$ due to the need to invert it. A BL/CC beam mapping configuration with weak independence among metrology beams results in poor conditioning of $dldx$, which can be seen more clearly by looking at the singular value decomposition (SVD) of $dldx$

$$SVD \text{ of } dldx = USV^t = \sum u_i s_i v_i^t \quad (5)$$

$$p_{inv}(dldx) = \sum v_i u_i^t / s_i \quad (6)$$

where u_i and v_i are singular vectors and s_i are singular values. When no metrology beams are completely correlated to each other, the matrix $dldx$ has full column rank and all singular values s_i are non-zero, but some weak correlation of metrology beams will result in very small singular values, which strongly magnify the wavefront estimation error since s_i in the denominators in equation (6). To have a suitable metric for quantifying the impact of sensor noise error on the wavefront estimate error, a scalar value called *Wavefront Error Multiplier (WEM)* is defined as

$$WEM = \text{mean}(\text{RMS}(dW^{\wedge})) / \text{mean}(|\eta|) \quad (7)$$

For a given LMET configuration, WEM can be easily computed according to equation (7) with a Monte Carlo simulation. The WEM value provides a multiplying factor of how much metrology measurement errors will be magnified, on average, to show up in the estimated system wavefront error. Our LUVOR laser metrology primary truss model places six BL around the edges of each hexagon shaped segment; the six metrology beams are mapped to three of the six CC near the perimeter of the secondary mirror (SM). Fig. 3 shows metrology beams from six segments, one on each ring, to the CC near SM. With CC locations fixed, when BL locations move around the segment edges, the WEM value can be seen to vary continuously. For the LUVOR primary metrology truss configuration, our model achieved a WEM value close to 6.5 when BL are placed near the center of each segment edge.

WEM can also provide a good estimate of closed-loop wavefront when taking into account of metrology sensing errors. If WFE_1 is the closed-loop wavefront residual assuming ideal metrology sensors with zero sensing error, and WFE_2 is the closed-loop wavefront residual with metrology sensing error η , then it can be shown, on average,

$$WFE_2 - WFE_1 = WEM * \eta \quad (8)$$

so WEM provides a convenient means of accessing controlled system performance in the presence of sensing errors.

3. LUVOR Primary Segment Edge Sensor Model and Eigen-Modes

We developed a generic edge sensor model for the LUVOR primary mirror with 120 segments. The sensor measurement model is generic in the sense that it does not involve specific sensor implementation details. The sensor model does calculations to measure changes of relative piston, gap and shear along an edge between segments. Two edge sensing spots are located at each edge between two neighboring segments.

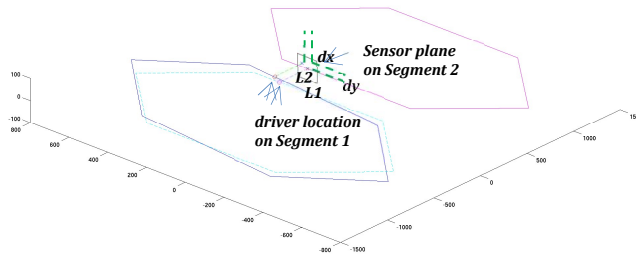


Figure 4: Edge sensor 3D measurement model

Each sensing spot consists of a *driver* on one segment and a *sensor* on the other segment. To compute edge sensor measurements, which does not imply an actual physical sensor implementation, a “beam” is launched from the driver spot on one segment and intersects with the sensor plane fixed on the other segment. The change of footprints of the driver beam on the sensor plane provides the changes of shear and relative piston when projected onto x and y axes of a sensor local coordinate frame, and the projection

onto z axis of the vector from a driver spot the origin of the sensor local coordinate frame provides the gap value. Fig. 4 Illustrates the edge sensing measurement model on a sensing spot between two segments. The segment on the sensor side does not move in this case while the driver segment is perturbed from its nominal position. dx is shear value which is the difference of beam projections to x axis, and, similarly, dy is the relative piston. Gap change is $L = L_2 - L_1$.

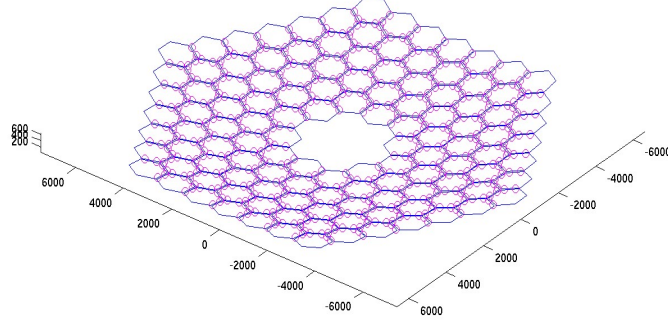


Figure 5: A set of 624 edge sensors along edges of 120 segments of LUVOIR primary mirror

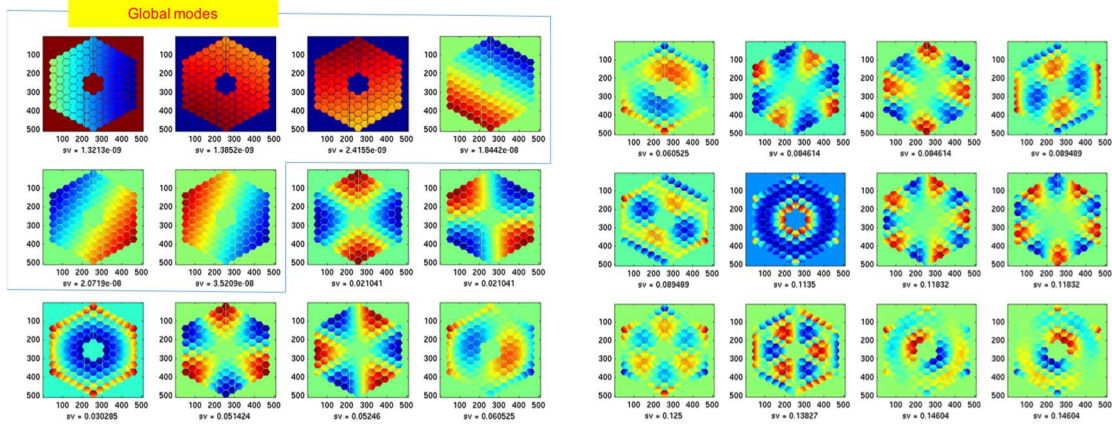


Figure 6: 24 weakest eigen-modes of 6DOF segment 3D edge sensors

The entire set of edge sensors on all 120 PM segments is shown in Fig. 5, where there are 312 edges with sensor measurements. On each edge of a segment with sensing spots, a driver is at one spot and a sensor is at the other spot, which correspond to a sensor and driver on the neighboring segment. Each sensing spot generates two 3D measurements of six values, with the total measurement values equal 1872. Denote $H = dedx$ the edge sensor rigid-body sensitivity matrix, with its column dimension = number of segments \times 6DOF = $120 \times 6 = 720$, and its row dimension = total sensor measurements = number of sensed edges \times 6 = $312 \times 6 = 1872$. Since edge sensors generate no response when the PM undergoes any rigid-body motion, which can be represented as a combination of three rotations and three translations with respect to a certain coordinate frame, H is a matrix with a null space of dimension six. To perform segment control with edge sensing, additional constraints or sensing mechanism is needed to generate segment state estimate.

The precision of wavefront control based on edge sensing, similarly to the control using metrology sensing, is determined by the wavefront error multiplier of the edge sensor system. It is useful to look at the *WEM* of edge sensors with respect to *mirror eigenmodes*. Edge sensors respond to each mirror eigenmode with a specific *measurement strength* and results in a corresponding *WEM* value. This can be illustrated treating edge sensors as a linear system, starting with a singular value decomposition of the sensitivity matrix H

$$H = dedx = USV^t = \sum u_i s_i v_i^t \quad (9)$$

where u_i and v_i are singular vectors and s_i are corresponding singular values. Denote de_i the sensor measurement of i -th eigen-mode, we have

$$de_i = dedx * v_i = s_i u_i \quad (10)$$

Define sensor measurement strength of i -th eigen-mode as the vector norm of de_i

$$|de_i| = s_i$$

so the singular value s_i is the edge sensor measurement strength of i -th eigen-mode. The wavefront map of the i -th eigen-mode can be generated by projecting v_i into the wavefront space

$$dw_i = dwdx * v_i \quad (11)$$

Fig. 6 shows wavefront maps of the 24 weakest eigen-modes along with the singular values (sv), and Fig. 7 shows the wavefront and singular value of the 24 strongest modes. The first six modes in Fig. 6 are indicated to be *global modes* corresponding to the mirror rigid-body motions with six DOFs, which should have zero singular value. The tiny singular values shown in Fig. 6 for the global modes are round-off residuals of numerical computation, which would otherwise be zero in exact mathematics. The singular modes constitute a null space of the sensitivity matrix $dedx$ that need to be removed with additional constraints or sensing for the purpose of segment state estimate and control.

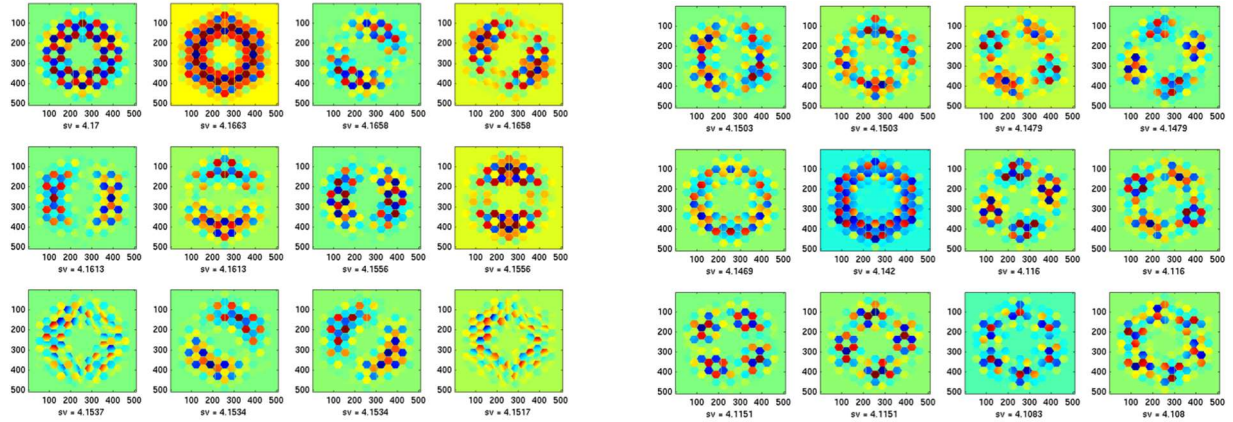


Figure 7: 24 strongest eigen-modes of 6DOF segment 3D edge sensors

Mode ordering could be some slightly different depending on sensor geometry, such as the distance between the driver and sensor. Beyond singular global modes, the edge sensors show some modes that generate very weak measurements. The weak modes, with small singular values, look similar to low-order Zernike type aberrations such as focus and astigmatism, and they contribute most significantly to the segment state estimation error in the presence of sensing errors. Let $d\hat{e}_i$ be the noisy edge sensor measurement of i -th eigen-mode with sensing error ε ,

$$d\hat{e}_i = de_i + \varepsilon$$

the estimated segment state $d\hat{x}_i$, with a simple least-square estimator, is

$$d\hat{x}_i = (dedx)_i^+ d\hat{e}_i = v_i u_i^t / s_i (de_i + \varepsilon) = v_i + (v_i u_i^t / s_i) \varepsilon \quad (12)$$

using de_i derived in equation(?). The second term in equation (12) is the segment pose estimation error of i -th eigen-mode due to sensing inaccuracy. The segment pose error multiplier of i -th eigen-mode, PEM_i is a vector of the size of total DOF of segments

$$PEM_i = \left[\left| \left(\frac{v_{i,1} u_i^t}{s_i} \right) \varepsilon \right| / |\varepsilon|, \left| \left(\frac{v_{i,2} u_i^t}{s_i} \right) \varepsilon \right| / |\varepsilon|, \dots \right]$$

Let $d\hat{w}_i$ be the estimated wavefront from $d\hat{x}_i$,

$$d\hat{w}_i = dwdx * d\hat{x}_i = dwdx * v_i + dwdx(v_i u_i^t / s_i) \varepsilon$$

the wavefront error multiplier of i -th eigen-mode WEM_i , with sensor noise ε , is a scalar value given by

$$WEM_i = \text{mean}(\text{RMS}(dwdx((v_i u_i^t / s_i) \varepsilon))) / \text{mean}(|\varepsilon|)$$

The total WEM of the edge sensors takes contributions from WEM_i of all mirror eigenmodes, with the most significant contributions coming from the weakest modes. Fig?? shows two WEM_i values for a weak focus mode and the strongest mode in Fig. 8. With the six global singular modes excluded, the total WEM of the edge sensors is 7.82, which implies, on average, a 7.82 pm wavefront error for 1 pm of edge sensing error.

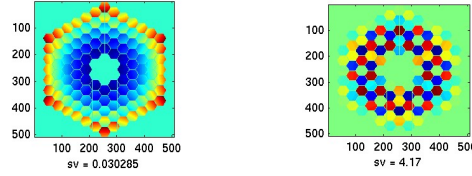


Figure 8: focus mode (left) with $WEM_i = 2.26$, strongest mode (right) with $WEM_i = 0.01879$

Capacitive edge sensors is an example of a physical implementation of the 3D segment edge motion sensing and measurement system we generically modeled in our LUVOIR edge sensor framework. A TMT-implemented parallel plate capacitor edge sensor is depicted in Fig. 9, where there is an upper capacitor formed by driver plate 1 and a sensor plate, and a lower capacitor formed by drive plate 2 and the sensor plate. The driver plates are installed under one segment, and the sensor plate under a neighboring segment, along a sharing edge. The relative tilt and translation motions of the segments change the effective areas and plate separations of the upper and lower capacitors, resulting in two sensor charge signals $R1$ and $R2$. Segment tilt, related to the dihedral angle θ as shown in Fig ??, and segment relative piston z can be computed from sensor readings. The relationship between θ and z and sensor readings can be derived, neglecting second-order terms [8], to reach the following equation

$$R = \frac{2A}{y} \left(k(B - f) + z + \frac{B^2 - f^2}{2y} \theta \right) \quad (13)$$

where, $R = R1 + R2$, and A is a function of electric and geometry constants.

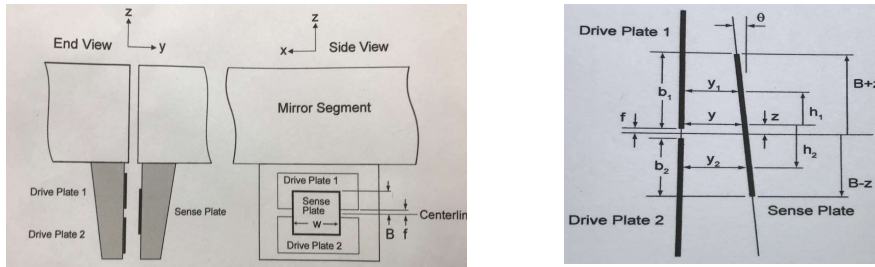


Figure 9: TMT capacitive sensor geometry and sensitivity model

In TMT implementation, the gap value y is independently measured, so with two sensors on each edge, the two sensor readings can be used through equation (13) to derive θ and z . To reduce sensor cost, TMT derives segment relative shear through the knowledge of gap y with the limitation of ignoring the effect of segment clocking.

4. Hybrid Mirror Segment Sensing with Truss Metrology and Edge Sensors

A more effective approach for primary mirror segment sensing is to combine the truss metrology and segment edge sensing. For instance, edge sensors are placed along all shared segment edges as shown in Fig. 9, and laser metrology sensors are placed on a few selected segments. First, this hybrid sensing arrangement removes the global modes encountered when using edge sensors only, and it also generates better (smaller) WEM values as an overall sensing system. Fig. 10 shows a set of hybrid sensing arrangements we studied. The segments with a tilt are the ones with six metrology beams around them. The rigid-body motions of these segments can be completely sensed and controlled by the truss metrology beams, so they act as “anchors” or references for other segments to be aligned around them through edge sensing and control. With hybrid metrology sensing, the joint sensitivity matrix can be formed by stacking the edge sensor sensitivity matrix $dedx$ and laser metrology sensitivity matrix $dldx$ for the selected segments in corresponding DOF columns. Symbolically, we write the hybrid sensitivity matrix $dmdx$ as

$$dmdx = dedx + dldx(\text{selected segments})$$

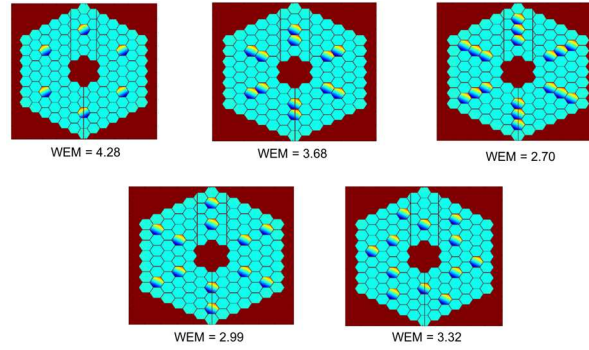


Figure 10: Hybrid sensing options and their WEM values. Segment with tilt have metrology sensing

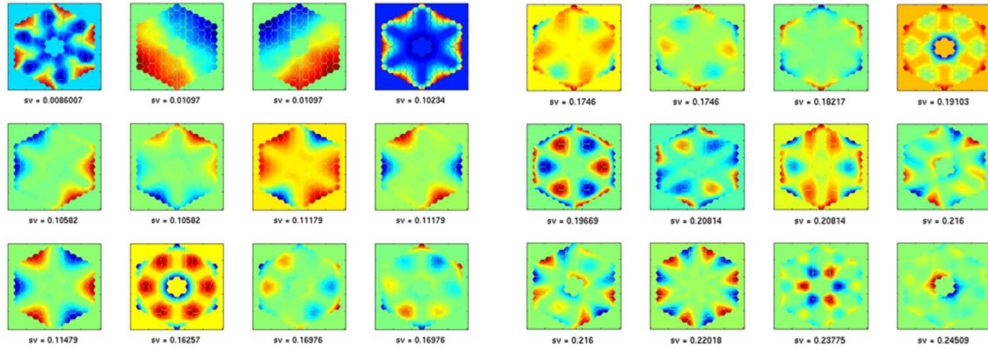


Figure 11: 24 weakest modes of the hybrid sensing configuration

WEM values can then be computed for the joint sensitivity matrices for each hybrid sensing option. Fig. 10 shows the WEM values for those configurations. With 12 or more segments having truss metrology constraints, the WEM values are around 3, which is noticeably better than using edge sensing alone. Fig. 11 shows the 24 weakest eigenmodes of the hybrid configuration with 12 segments having truss metrology beams.

5. LUVOIR Primary Mirror Stabilization with Hybrid Sensing and Control

We performed simulation and analysis of LUVOIR primary mirror segment stabilization with hybrid segment sensing and control. The state estimation and wavefront control approach is similar to what was discussed in Redding 1991 paper [2] and implemented in CCAT [3]. Again let $\frac{dm}{dx}$ be the hybrid sensitivity matrix, n be edge and metrology sensing error vector, and x be the segment rigid-body state vector, the measurements m can then be written as

$$m = \frac{dm}{dx} * x + n$$

Suppose some a priori knowledge of the statistics of segment initial alignment errors is available, and some a priori knowledge of edge sensing and metrology sensing errors can be estimated, then both can be incorporated into the segment state estimation process. Thus let X_0 be the covariance matrix of segment initial alignment errors, and R be the covariance matrix of sensor measurement errors, a segment state estimator can be derived by minimizing the following objective function J in terms of x .

$$J = \frac{1}{2} [x^t X_0^{-1} x + \left(m - \frac{dm}{dx} x\right)^t R^{-1} \left(m - \frac{dm}{dx} x\right)] \quad (14)$$

Setting dJ/dx to zero, we get a least-square estimate of the segment state x_{est} . Absent from sensor measurement errors n , we have

$$x_{est} = K * m = K * \frac{dm}{dx} x$$

where

$$K = P^{-1} \frac{dm}{dx} R^{-1}, \quad P = X_0^{-1} + \left(\frac{dm}{dx}\right)^t R^{-1} \frac{dm}{dx}$$

With sensor measurement errors included, the segment state estimate is

$$x_{est} = K * \frac{dm}{dx} x + K * n$$

The two terms in equation (?) for the cost function J balances each other in the least-square procedure depending on the ratio of X_0 and R . The first term, essentially a penalty on the state x , adds a soft constraint on the segment motions in the estimated state. If, say, we had the knowledge that segment errors are small, implying the covariance errors X_0 would be small and hence its inverse would large, the first term of J then puts a large penalty on it, which is equivalent to a constraint on segment motions estimate, and would generally influence the search for a state estimation by the least-square optimizer. On the other hand, if our knowledge of segment motions is rather poor, thus assuming a very large covariance X_0 , which effectively drops the first term from J , and therefore there will be little constraint on x when searching for a state estimate. If the sensing errors are known to be large, a small R^{-1} (relative to X_0) implies that $\left(m - \frac{dm}{dx} x\right)$ doesn't need be too small for the state estimate x , which tends to reduce noise magnification effect on wavefront error by the weak modes of $\frac{dm}{dx}$. With the state estimate x_{est} , the estimated wavefront can be computed using the linear wavefront model

$$w_{est} = w_t + \frac{dw}{dx} x_{est} \quad (15)$$

where $\frac{dw}{dx}$ is the linear sensitivity matrix of LUVOIR wavefront with respect to segment state x , w_t is the known target or desired wavefront when segment state errors is zero. The estimated wavefront w_{est} can then be minimized or driven to the target wavefront w_t in a wavefront control process. The true linear wavefront w can be written as

$$w = w_t + \frac{dw}{dx} x$$

where x is the true segment state. The *estimated* controlled wavefront can be written as

$$w_{est,c} = w_t + \frac{dw}{dx} x_{est} + \frac{dw}{du} u \quad (16)$$

where u is the vector of controllable part of state x . The expression in (**) shows the control acts upon the estimated wavefront w_{est} instead of the true wavefront which is unknown. Setting $w_{est,c} = w_t$, we get the state control vector

$$u = -\left(\frac{dw}{du}\right)^+ \frac{dw}{dx} x_{est}$$

where $()^+$ is the pseudo-inverse operator used to provide a least-square solution. After the state control is applied to the actual system, the true controlled wavefront is

$$w_c = w_t + \frac{dw}{dx} x - \frac{dw}{du} \left(\frac{dw}{du}\right)^+ \frac{dw}{dx} x_{est} \quad (17)$$

If all elements in the system are controllable, that is $\frac{dw}{du} = \frac{dw}{dx}$, we have

$$w_c = w_t + \frac{dw}{dx} (x - x_{est})$$

In this case, the control would restore the system to its target wavefront w_t if the state estimate is perfect ($x = x_{est}$). In reality, the state estimate will be imperfect due to sensing errors, and generally the control vector u is in a subspace of system state space x (with non-controllable optical elements) and the presence of other non-controllable errors (such as element surface errors), all contributing to the post-control (closed-loop) wavefront errors.

We now discuss several simulation exercises of LUNVOR primary mirror segments alignment by means of segment state estimation and wavefront control using the sensing and control framework outlined above. In the first step of the simulation, random rigid-body (pose) errors are applied to each of 120 primary mirror segments to generate an initial segment state vector x of dimension 720 ($=120 \times 6$), with segment having three rotation and three translation errors with respect to its local coordinate frame. A hybrid truss metrology and edge sensing strategy is used to generate an estimated segment state x_{est} . Truss metrology measurements, using the secondary mirror rim as reference, are implemented on 12 selected segments, with six metrology beams on each segment. Edge sensors are implemented on all 120 segments, with two edge sensing spots along each edge of two neighboring segments. The hybrid sensing configuration is as shown in the second image of first row in Fig. 10, with a WEM of 3.68. We start with an ideal sensing case with zero sensing errors, applying random segment rotation errors of 0.5 micro-radian standard deviation and random segment translation errors of 0.5 micron standard deviation, all uniform distributed. The *nominal* (un-perturbed) wavefront and the wavefront with segment rigid-body errors are shown in Fig ?? below

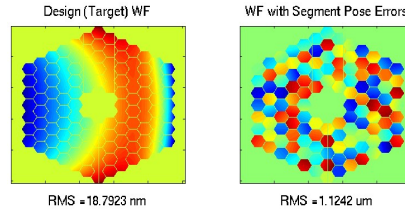


Figure 12: Design (target) wavefront and wavefront with pose errors

The nominal wavefront with 18.79 nm RMS, is the design residual wavefront of LUNVOR 120-element architecture A telescope, which includes a primary, a secondary, a tertiary and a fast-steering mirror. The wavefront image on the right in Fig. 12 is the result of a single realization of random segment pose errors, with about 1.1 micron RMS. Following the control scheme discussed earlier, a wavefront estimate w_{est} is generated using x_{est} and linear wavefront model (16), a 6DOF segment control is then performed to drive the (estimated) wavefront towards to the target wavefront (the first image in Fig. 12). The post-control wavefront is shown in Fig. 13.

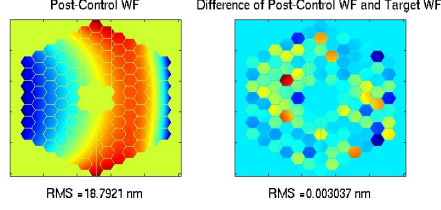


Figure 13: Closed-loop wavefront, zero sensing error

With zero metrology and edge sensing errors, the segment state estimate x_{est} should be very close to the true state x , with the difference contributed only from computational precision errors of the state estimator. Since the control is applied to 6DOF of all segments and there is no other error sources elsewhere in the system, the post-control wavefront should be very close to the target wavefront, as shown the controlled wavefront and the difference between the controlled and the target wavefront in Fig. 13. Next we add sensing errors to the metrology and edge sensing. Using sensing errors generated with a standard deviation of 1.0 nanometer and applied to both metrology and edge sensor measurements, the state estimate based wavefront control performance is shown in Fig. 14. The result shows the controlled wavefront RMS is slightly larger than the target wavefront (left image above), as expected. The difference wavefront map (right image above) more clearly reveals the effect of sensing errors, which shows the segment state estimation errors on the controlled wavefront errors, and the random distribution of sensor errors results in the random nature of the wavefront control error distribution. Note that the controlled wavefront *error* (right image in Fig. 14) is now 3.3 nm RMS versus the sensing error standard deviation of 1.0 nm. On average, the ratio of controlled wavefront error and the sensing error should be close to the wavefront error multiplier as indicated by equation (8); in our current simulation a hybrid sensing configuration with a WEM of 3.68 is used. In the next experiment, the sensing error is reduced to 100 picometer, and the results from one random realization of sensing errors are shown in Fig. 15

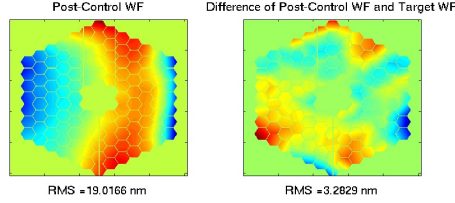


Figure 14: Closed-loop wavefront, 1.0 nm sensing errors

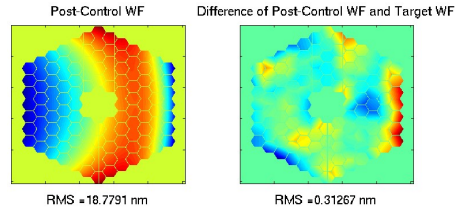


Figure 15: Closed-loop wavefront, 100 pm sensing errors

The controlled wavefront error (right image above) is reduced to 0.31 nm RMS, compared to 3.28 nm RMS when sensing error is 1 nm. The almost linear increase of controlled wavefront error with sensing error is expected since the sensing error is an additive noise in the measurement equation and the controlled wavefront error in our simulation results entirely from metrology and edge sensing errors. To enable exoplanet sciences, LUVOIR coronagraph instrument needs 10d-10 contrast and pico-meter level wavefront errors, which requires metrology and edge sensing accuracy at pico-meter level. Using 10 pico-meter sensing errors, the wavefront control performance is shown in Fig. 16.

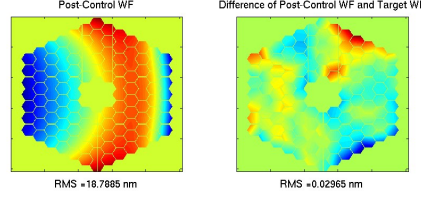


Figure 16: Closed-loop wavefront, 10 pm sensing errors

Again, the post-control wavefront error is reduced by an order of magnitude to 29 pico-meter, as expected. The results shown above are from one realization of a random distribution of sensing errors with a particular standard deviation, and the initial segment pose errors are drawn from a random distribution but do not change with sensing errors to make it easier to compare the effects of sensing errors. To show the variation of open and closed-loop wavefront with random segment poses and sensing errors, a Monte Carlo simulation of 200 runs is performed, with sensing error standard deviation at 10 pm. The wavefront plots are shown in Fig. 17.

Let dW be the difference between controlled wavefront and target wavefront, we can compute the average of the ratio of dW and sensing errors in the Monte Carlo runs, which turns out to be 3.72. The hybrid sensing configuration we use for the simulations has a *WEM* of 3.68. The two values being close is also an experimental verification of equation (*).

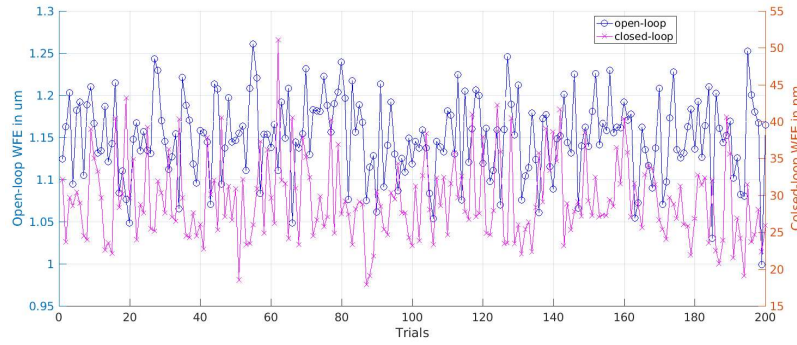


Figure 17: Open and closed-loop wavefront, 200 Monte Carlo runs, sensing error 10 pm

The segment state and wavefront estimators have different sensitivity levels to segment out-of-plane and in-plane motions; out-of-plane motions include segment tip, tilt and piston, and in-plane motions include segment clock and translations. The weaker sensitivity of wavefront to segment in-plane motions led us to investigate the possibility of measuring segment in-plane motions at a lower accuracy while maintaining high measurement accuracy for segment out-of-plane motions, and achieve comparable closed-loop wavefront performance to that of measuring both in-plane and out-of-plane segment motions with high accuracy. In the hybrid metrology and edge sensing for LUVOR primary mirror segments, for example, high accuracy measurements are used for segment truss metrology and edge relative piston sensing, while low accuracy measurements are used for segment gap and shear sensing. We experimented several sensing error distributions to show the variations of closed-loop wavefront performance for isotropic sensing errors and anisotropic sensing errors, with results shown in Fig. 18. Again, 12 metrology segments are used as before. From Fig. 18, when applying 10 pico-meter (pm) sensing errors to all metrology and edge-sensing measurements, the closed-loop wavefront is 29.65 pm after sensing and control (upper left image). When applying 100 pm sensing errors to all metrology and edge-sensing measurements, the closed-loop wavefront is 226.6 pm (upper right image), with a linear scaling as expected from our sensing error and control models. Next we increase the in-plane edge sensing measurement (gap and shear) error to 100 pm while keeping the metrology and edge relative piston measurement error at 10 pm, the closed-loop wavefront rises only modestly to 42.9 pm (lower left image) compared to the case of isotropic sensing error of 10 pm. When the in-plane motion measurement error

is further increased to 1000 pm and metrology and piston measurements still at 10 pm, the closed-loop wavefront is increased to 203.8 pm (lower right image). These results suggest that when in-plane measurement error is increased by one order of magnitude while keeping the same out-of-plane measurement error, the closed-loop wavefront deterioration is quite limited, but a further significant increase of in-plane measurement error would result in large closed-loop wavefront residuals. The results

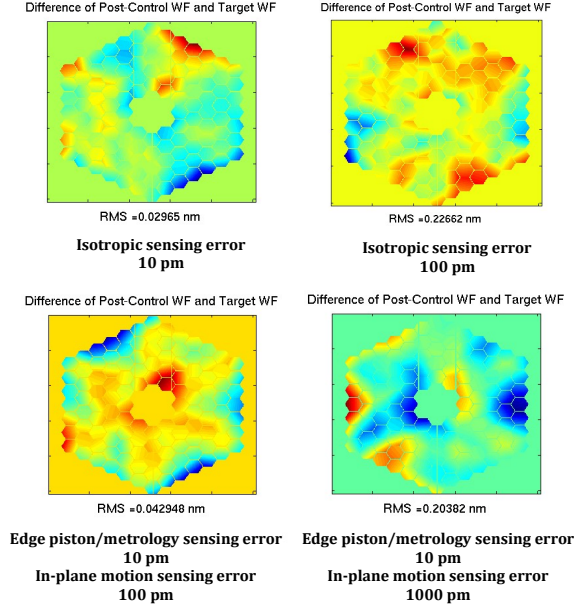


Figure 18: Closed-loop wavefront with isotropic and anisotropic sensing errors

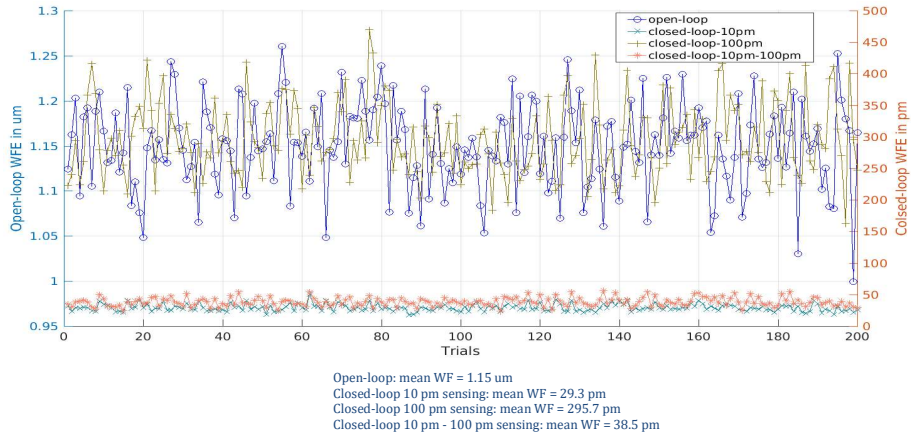


Figure 19: Monte Carlo WFC simulations 10-100 nm sensor error distributions

in Fig. 18 are from a snapshot of random sensing errors. Fig. 19 and Fig. 20 show the results from 200 Monte Carlo runs with indicated sensing errors as standard variations used to generate random measurement errors. The mean of open-loop wavefront is 1.15 μm due to primary segment rigid-body pose errors. The mean values of closed-loop wavefront in each case are consistent with the results and discussions we presented above with a single realization of sensing errors.

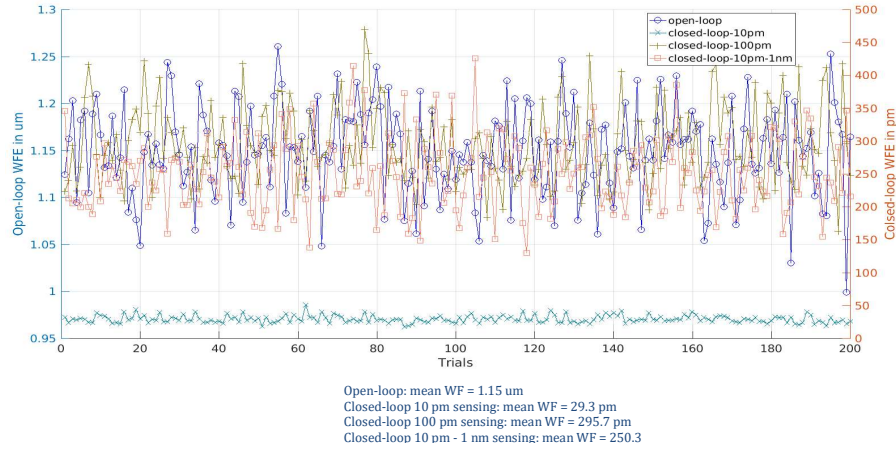


Figure 20: Monte Carlo WFC simulations 10-1000 nm sensor error distributions

6. Conclusion

A LUVOR primary segment truss metrology sensing model and an edge sensing model are presented, in reference to the LUVOR Architecture Option A with a 15-meter primary of 120 segments. A hybrid segment motion sensing strategy is proposed that combines truss metrology and segment edge sensing, with metrology beams placed on a small set of segments and edge sensors on all segments. It is shown the hybrid sensing approach removes the non-observable global modes present in the 6DOF edge sensor model, generates small wavefront error multipliers for sensor errors, and enables a robust 6DOF segment state estimation and wavefront control.

Numerical simulation results using the hybrid sensing approach, 6DOF segment state estimation and wavefront control are discussed. It is shown that with random segment initial rigid-body errors of several microns RMS, the 6DOF segment state estimation and subsequent control on the estimated wavefront can restore the LUVOR system very close to its design wavefront when sensor errors are negligible. It is also shown, with Monte Carlo simulations, the closed-loop wavefront with sensor errors is on average the product of sensor architecture WEM and the mean of sensor errors, as can be theoretically established. Finally, it is shown from simulations that when the sensor accuracy measuring segment in-plane motions is an order of magnitude lower than that of measuring segment out-of-plane motions (including truss metrology), the degradation of closed-loop wavefront is quite limited

References

- (1) D. Redding: LUVOR Technology Development, NASA LUVOR WG Document Ch. 11. (2018)
- (2) D. Redding, B. Breckenridge, Ken Lau, G. Sevaston, M. Levine and S. Shaklan, *Segmented Mirror Figure Control for a Space-Based Far-IR Astronomical Telescope*, SPIE Vol. 1489, Structures Sensing and Control, 1991 / 201
- (3) J. Lou, A. Kissil, D. Redding, and M. Bradford, S. Padin, D. Woody, "Modeling a Large Submillimeter-Wave Observatory," SPIE Optics+Photonics, San Diego, 2010, Vol 7733-74
- (4) F. Shi *et al.*, "Low Order Wavefront Sensing and Control for WFIRST-AFTA Coronagraph," JATIS, Vol 2 (1), (2016).
- (5) Justin Moore: OBWS, [Moore2017] D. Moore, "Out of Band Wavefront Sensing for LUVOR Coronagraph," JPL Presentation URS267430 (2017).

- (6) D. Redding, F. Shi, S. Basinger, D. Cohen, J. Green, A. Lowman, C. Ohara, *Wavefront Sensing and Control for Large Space Optics*, IEEE AC paper #1720, 1-8-2003
- (7) Joel Nissen, Alireza Azizi, Feng Zhao, Shannon Kian G. Zareh, Shanti R. Rao, Jeffrey B. Jewell
 “Laser metrology for ultra-stable space-based coronagraphs,” *Proceedings UV/Optical/IR Space Telescopes and Instruments: Innovative Technologies and Concepts VIII*, Volume 10398, SPIE Optics+Photonics August 6-10 2017, San Diego, CA.
- (8) Chris Shelton, “Advances in Edge Sensors for the Thirty Meter Telescope Primary Mirror,” Proc. SPIE 7012, 701210 (2008).
- (9) David P. Burt, Phillip S. Dobson, Kevin E. Docherty, Christopher W. Jones, Richard K. Leach, Stephen Thomas, Jonathan M.R. Weaver, and Yuan Zhang, “Aperiodic interferometer for six degrees of freedom position measurement,” *Optics Letters* Vol. 7, No. 7 (2012).
- (10) F. Zhao, “Picometer laser metrology for the Space Interferometry Mission (SIM),” IEEE Conf. on Lasers and Electro-Optics (2004)